Activity Correlation Imaging: Visualizing Function and Structure of Neuronal Populations

Stephan Junek,[†] Tsai-Wen Chen,[†] Mihai Alevra,[†] and Detlev Schild[†‡*]
[†]Department of Neurophysiology and Cellular Biophysics, and [‡]Deutsche Forschungsgemeinschaft Research Center for Molecular Physiology of the Brain, University of Göttingen, Göttingen, Germany

ABSTRACT For the analysis of neuronal networks it is an important yet unresolved task to relate the neurons' activities to their morphology. Here we introduce activity correlation imaging to simultaneously visualize the activity and morphology of populations of neurons. To this end we first stain the network's neurons using a membrane-permeable [Ca^{2+}] indicator (e.g., Fluo-4/AM) and record their activities. We then exploit the recorded temporal activity patterns as a means of intrinsic contrast to visualize individual neurons' dendritic morphology. The result is a high-contrast, multicolor visualization of the neuronal network. Taking the *Xenopus* olfactory bulb as an example we show the activities of the mitral/tufted cells of the olfactory bulb as well as their projections into the olfactory glomeruli. This method, yielding both functional and structural information of neuronal populations, will open up unprecedented possibilities for the investigation of neuronal networks.

INTRODUCTION

Analysis of neuronal network function would be drastically improved by a technique that allows simultaneous measurement of both the activity of every neuron in a network and its morphology and projection pattern. Significant advances in one or the other direction have been made recently. On the one hand, transgenic strategies for combinatorial expression of fluorescent proteins allow the visualization of the detailed morphology of neuronal populations with excellent contrast (1) but fail to detect the functional activities of the neurons labeled. On the other hand, functional imaging using bolus loading of membrane-permeable [Ca^{2+}] indicators allows an almost complete visualization of neuronal activity at cellular resolution (2–4). However, because this technique unspecifically stains every neuron in the network, it does not give sufficient contrast to visualize the fine processes of individual neurons (5,6). Alternatively, [Ca^{2+}] indicators can be loaded into a sparse subset of neurons to enable a simultaneous visualization of activity and fine neuronal structures (6), but this approach is intrinsically limited to imaging a small fraction of cells. Combining the advantages of these approaches would provide an invaluable tool for neuroscience research.

Here, we propose a method that allows high contrast visualization of neuronal circuitry during large-scale functional imaging experiments using bolus loading of membrane-permeable [Ca^{2+}] indicators. Specifically, we derive image contrast from the diversity of temporal activities recorded with [Ca^{2+}] sensitive dyes, rather than from the differences in fluorescence intensities. This allows us to visualize individual fine neuronal processes even when the entire neuronal circuit is unspecifically stained with fluorescence dye. This method develops its full potential when combined with fast image acquisition and provides a multicolor visualization of neuronal networks during functional imaging of brain tissue.

MATERIALS AND METHODS

Slice preparation and staining of tissue

The preparation of brain slices of tadpoles of *Xenopus laevis* (stage 51–54; 7) as well as the bulk staining with Fluo-4/AM or Fura-2/AM were done as previously described (8–10), as approved by the Göttingen University Committee for Ethics in Animal Experimentation. For 3D imaging, a solution containing 100–500 μM Fluo-4/AM was pressure-injected at a depth of ~70 μm using patch pipettes (6–8 MΩ, 50–100 hPa for 1–5 min) into two sites per bulb hemisphere (adopted from 2,5).

Microscopy

Confocal volume imaging was performed using a custom-built line-scanning microscope at an acquisition rate of 500–700 ms per stack (18–20 images per stack). An argon ion laser (Laser Technologies, Kleinostheim, Germany) at 488 nm was used as light source. The following filters were used for excitation, emission, and as dichroic mirror: z488/10, HQ532/70, and z488rdc, respectively (AHF Analysentechnik, Tübingen, Germany). Emission light was collected using a linear charge-coupled device (CCD) camera, with the width of the pixel serving as the confocal aperture (512 × 1 pixels, 14 × 14 μm each, Atmel, San Jose, CA). The focal lengths of the scan lens and the lens in front of the camera were 80 mm and 50 mm, respectively. The pixel width thus corresponds to 0.55, 0.74, and 1.18 airy units for the 63×/0.95, 40×/0.8, and 25×/0.8 objective, respectively (for λ_{em} = 500 nm). Scan mirror (GSI Luomincs, Billerica, MA), piezo actuator (PI, Karlsruhe, Germany), shutter, and camera trigger were controlled via custom software written in C++. For standard confocal imaging, we used an Axiovert 100M equipped with a laser-scanning unit LSM 510 (Zeiss, Jena, Germany). For Fura-2 measurements, we used an upright microscope (Axioskop 2, Zeiss, Göttingen, Germany) equipped with a Fura-2 filter set (dichroic, FT425; emission filter, 510/80). Excitation light at 380 nm was selected from a xenon lamp using a custom built monochromator (8,9). Fluorescence images were taken using a frame-transfer, back-illuminated CCD camera (Micromax, Visitron, Munich, Germany). The following objectives

Submitted October 7, 2008, and accepted for publication December 1, 2008.

*Correspondence: dschild@gwdg.de

Stephan Junek and Tsai-Wen Chen contributed equally to this work.

Editor: Alberto Diaspro.

0006-3495/09/05/3801/9 $2.00

doi: 10.1016/j.bpj.2008.12.3962

were used as indicated in the text: 25× LD LCI Plan-Apochromat NA 0.8 W; 40× Achroplan 0.8 W; 63× Achroplan 0.95 W; 40× C-Apochromat 1.2 W; 10× Plan-NeoFluar 0.3 (all Zeiss, Jena, Germany).

Patch clamp injection

Patch clamp was performed using an EPC7 plus amplifier (HEKA, Lambrecht/Pfalz, Germany) and pipettes with a series resistance between 8 and 12 MΩ. Alexa Biocytin 532 (Invitrogen, Karlsruhe, Germany) was added to the intracellular solution (in mM: 2 NaCl, 11 KCl, 2 $MgSO_4$, 80 K-Gluconat, 10 Hepes, 0.2 EGTA, 2 Na_2ATP, 0.1 Na_2GTP). After breaking the seal, the cell was held at −65 mV for 1 min to allow diffusion of the dye into the cytosol.

Data analysis

All data analysis was performed using custom software written in MATLAB (The MathWorks, Natick, MA). A bleach correction was first performed for all pixels by subtracting a linear trend from each pixel's time trace. The reference traces were obtained by averaging the fluorescence intensities across individual regions of interest (ROIs) for each time point.

To facilitate the selection of ROIs, a "neighborhood correlation map" was obtained by calculating the cross correlation between the fluorescence signals of a pixel to those of its immediate neighbors and then displaying the resulting value as a grayscale map (11). As physiological responses often give similar signals in adjacent pixels, this method specifically highlights those pixels. In contrast, pixels that contain only noise show uncorrelated traces and thus appear dark in the cross correlation map (10). The ROIs were then selected semiautomatically, on the basis of the correlation between the time traces of a manually selected pixel and the time traces of the pixels in a certain neighborhood (~20 × 20 × 20 μm^3) around this pixel (11,12).

The correlation map for the j^{th} ROI was then created by calculating the correlation coefficients between the reference trace $r_j(t)$ and the time traces $v_i(t)$ of each pixel. The i^{th} pixel in the j^{th} correlation map gets thus assigned the value

$$c_{ij} = \frac{\sum_{t=1}^{T} \left(v_i(t) - \overline{v}_i\right)\left(r_j(t) - \overline{r}_j\right)}{\|v_i(t) - \overline{v}_i\| \cdot \|r_j(t) - \overline{r}_j\|},$$

with T being the number of time points of the observation, and $\|\cdot\|$ denoting the 2-norm of the respective vector. For experiments where $[Ca^{2+}]$ signals were sampled at a higher rate (5–10 Hz in epifluorescence imaging), a slow baseline drift (calculated by smoothing the trace with a Hanning filter, window length 8 s) was subtracted from the reference trace before calculating the correlation maps. This procedure emphasizes the rising phases of the $[Ca^{2+}]$ signals and is effective in reducing nonspecific correlations caused by the slow decay of $[Ca^{2+}]$ signals. For experiments with a lower sampling rate (<2 Hz in 3D volume imaging), this procedure is often unnecessary and therefore not applied. Displayed correlation maps were in some cases (see Fig. 5 *b*) mildly Gauss-filtered (width <1 pixel).

Computer simulation

Computer simulation experiments were performed using MATLAB. $[Ca^{2+}]$ signals $f(t_k)$ were simulated as the sum of individual events each being characterized by a sudden rise followed by an exponential decay to mimic the intracellular $[Ca^{2+}]$ waveform (12). The onset timing of each event was determined according to a Poisson point process. A pixel's signal $y(t_k)$ was modeled as a scaled version of the cells' $[Ca^{2+}]$ signal, plus noise:

$$y(t_k) = \alpha f(t_k) + n(t_k), \text{ here } \sum_k (f(t_k) - \overline{f})^2 = 1.$$

The standard deviation σ_n of the noise added was determined by $\sigma_n = \alpha/SNR$, where SNR is the predefined signal/noise ratio (SNR) value.

RESULTS

Principle of activity correlation imaging

We imaged the spontaneous $[Ca^{2+}]$ activities in the mitral/tufted (M/T) cell layer of the olfactory bulb (OB) of *Xenopus* tadpoles using bulk loading of membrane-permeable $[Ca^{2+}]$ indicators (Fig. 1 *a*). Within these image series individual pixels carry time-dependent signals that reflect the $[Ca^{2+}]$ fluctuation of the imaged structures. To visualize the spatial

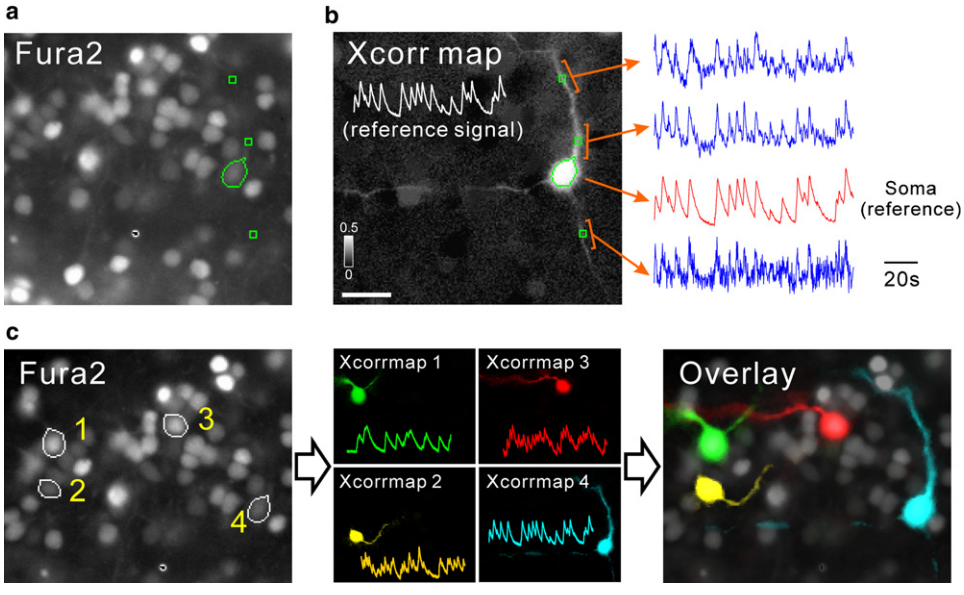

FIGURE 1 Principle of ACI. (*a*) A fluorescence image of the *Xenopus* OB stained with $[Ca^{2+}]$ indicator Fura-2. The processes of the neurons are hardly visible due to a lack of contrast. (*b*) A pixel-based map of cross correlation values (Xcorr map) calculated with respect to the signal of the marked soma (the reference signal). In this map, the brightness of individual pixels encodes the degree of cross correlation between the pixels' fluorescence signals and the reference signal. Three processes of the cell can be visualized in this map because of their correlated $[Ca^{2+}]$ signals (*right*, the traces represent averaged signals of the bracketed areas). (*c*) Maps of correlation values for four neurons (marked in the raw Fura-2 image, *left*), coded with different colors (*middle*), and overlayed on the raw fluorescence image (*right*). The $[Ca^{2+}]$ signals used to generate the maps are shown on the corresponding correlation maps (*middle*). Scale bar, 20 μm.

distribution of a particular time trace we constructed activity cross correlation maps (see Methods), in which the brightness of a pixel encodes the cross correlation value of the pixel's signal to a predetermined reference signal (e.g., the $[Ca^{2+}]$ signal of a particular cell soma). The correlation map mostly showed a brightly labeled soma (from which the reference signal was taken) on a relatively dark background reflecting the fact that the spontaneous $[Ca^{2+}]$ activities of most cells were uncorrelated (27). Interestingly, the correlation maps also revealed structures resembling neuronal processes (Fig. 1 *b*), not seen in the raw fluorescence image (Fig. 1 *a*).

Using different patterns of spontaneous activity as reference traces produced different correlation maps (Fig. 1 *c*, *middle*). By assigning different colors to the resulting maps, we could visualize the neuronal circuits with a markedly enhanced contrast (Fig. 1 *c*, *right*). We term this procedure of contrast generation ''activity correlation imaging'' (ACI).

Using a 40× (NA = 0.8) objective, the correlation maps mostly revealed neuronal processes located relatively close to the respective somata (Fig. 1 *c*). To clarify whether this was due to the distal processes leaving the focus or to the $[Ca^{2+}]$ signal correlations decreasing along the processes, we performed ACI using a low NA objective (10×/0.3) with a more extended focal depth. Now the correlation maps revealed longer pieces of neuronal processes and, in some cases, we could trace mitral cell dendrites from their somata to their glomerular endings located >150 μm away from the soma (Fig. S1 in the Supporting Material). Moreover, secondary dendrites could be clearly identified (Fig. S1).

ACI can thus visualize processes and guide the measurement of signals from a neuron's processes even when they are located far away from the soma and not visible in the raw fluorescence image (Fig. S1). However, the experiments presented so far have two serious limitations. First, small numerical apertures sacrifice photon detection efficiency and *z*-resolution, and second, the observable volume is limited to the objective's depth of focus (a few micrometers).

Fast confocal line scanning for ACI in 3D

We therefore decided to extend ACI to time series of 3D image stacks, which would allow the observation of a significantly thicker fraction of the network at high resolution and high photon efficiency. To enable a global correlation analysis to all pixels in 3D, one has to ensure that the signals of all pixels can be regarded as being acquired at approximately the same time. This simultaneity would require the acquisition of an entire 3D image stack within a short time window. We thus designed and built a confocal scanning microscope where a line of excitation light (instead of a point) is projected onto the sample (Fig. 2). The object is scanned in one direction only, perpendicular to the excitation line. Provided a fast sensor and acquisition system, much higher frame rates can thus be achieved. A number of line-scanning realizations have been described (13–15), most often though with applications to nonfluorescent samples or nonbiological specimens.

Time-lapsed 3D imaging usually requires acquisition of a large number of images, which is typically accompanied by significant bleaching of the fluorescent dye. We thus optimized our design for maximum efficiency in the emission pathway by reducing the number of optical elements. The optical design is shown in Fig. 2. The collimated laser light is focused into a line on the scan mirror by use of a cylindrical lens (Fig. 2, *a* and *b*). Scan lens and tube lens project this line into the back-aperture of the objective, which creates a perpendicular line in the object plane. Behind the dichroic mirror, a single lens focuses the light onto the linear CCD array. We took the pixel width of the CCD line as the confocal aperture. Although this design sacrifices the ability to adjust the thickness of the optical section, it maximizes photon efficiency by omitting the associated pinhole optics. Fig. 2 *b* depicts the light propagation in *x*- and *y*-direction for excitation (*green*) and emission (*red*) in a schematic way. Whereas the light path in *x*-direction (*light colors*, *broken lines*) is identical to the propagation in a conventional confocal microscope (except the emission pinhole optics), the *y*-direction resembles the design of a widefield microscope, with a focus in the backfocal plane of the objective and an extended detector. The *z*-position of the object plane was adjusted by moving the objective with a piezo-driven actuator. In this way image stacks can be obtained at a rate up to 10 Hz. We typically used acquisition times of ~500 ms per stack.

ACI reveals network function and structure in 3D

We demonstrate the potential of ACI together with fast confocal 3D scanning by using calcium imaging of OB tissue slices from *X. laevis* tadpoles (25×/NA 0.8 W objective). Fig. 3 *a* shows the mean projections over time for three out of 18 *z*-slices, with the reference ROI (glomerulus encircled) and its time trace superimposed. On the basis of this reference trace, correlation values for all pixels in the observation volume were calculated, resulting in a stack of correlation maps (Fig. 3 *b* shows the maps of the *z*-positions corresponding to Fig. 3 *a*). Whereas each map by itself only shows some parts of the neuronal structures, their overall connectivity is revealed either by a maximum *z*-projection (Fig. 3 *c*), or 3D volume rendering (Movie S1). Although the maps contain a number of neurons, the ''labeling'' is sparse enough to identify the neuronal processes and assign them to their respective somata. As long as the dendrites don't leave the observation volume, the connectivities between somata and glomerulus can be established unambiguously.

As individual neurons show specific activity patterns, we were able to obtain many correlation maps using different ROIs and reference signals. Fig. 3 *d* shows six maps each

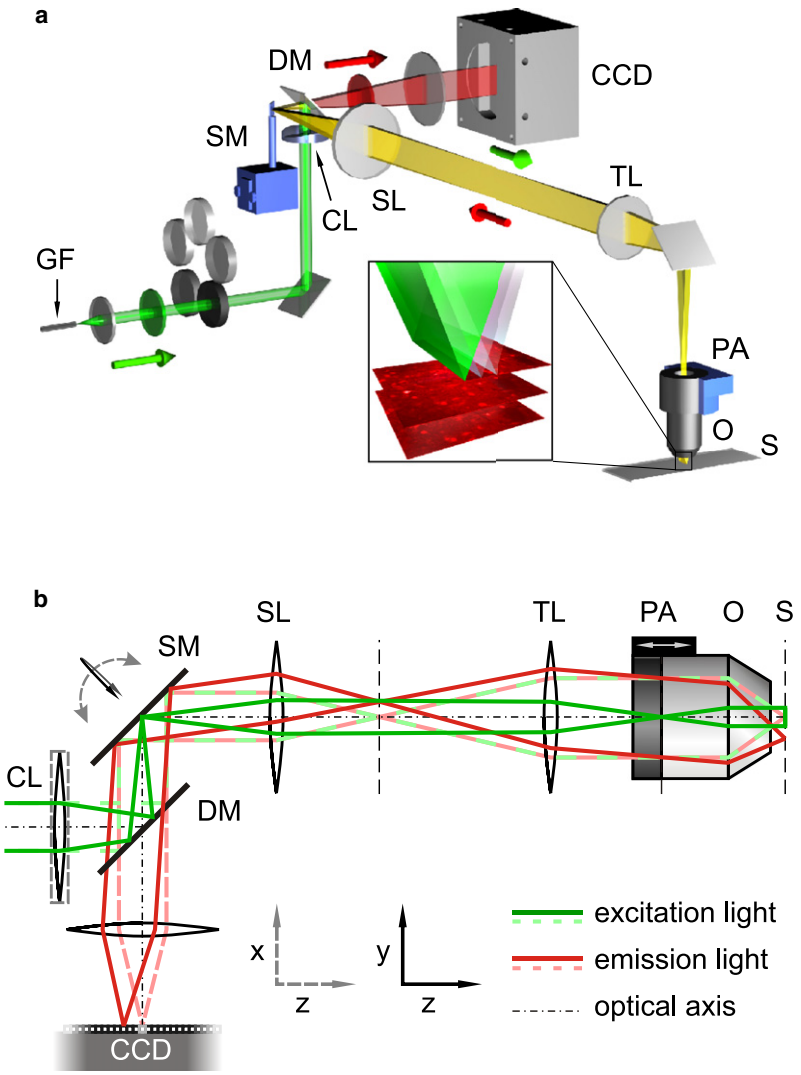

FIGURE 2 Microscopic setup. (*a*) Schematics of optical design. Laser light (488 nm) issuing from a glass fiber is collimated and filtered. A cylindrical lens focuses the Gaussian beam onto a line on the scan mirror. An image of this line is projected into the backfocal plane of the objective, resulting in a perpendicular line in the object plane. Moving this line in *y*-direction scans the object in 2D. Scans in 3D (*inset*) can be achieved by additional objective positioning (*z*) using a piezo actuator. The light emitted from the sample is gathered by the objective's aperture. It passes the tube lens, the scan lens, the dichroic mirror, and emission filter, and is then imaged by a single lens onto a linear CCD array. Note the absence of a slit aperture in front of the camera. Colored arrows indicate the propagation for excitation (*green*) and emission (*red*) light. (*b*) Schematics of light propagation in *x*- and *y*-direction for excitation (*green lines*) and emission (*red lines*). Glass fiber, collimator, and filters are omitted for clarity. In *x*-direction (*light colors*, *broken lines*), the setup is identical to a standard confocal microscope, the emission pinhole being replaced by the width of the CCD line detector. In *y*-direction (*dark colors*, *solid lines*), a cylindrical lens introduces a focus on the scan mirror and subsequently in the back-focal plane of the objective, comparably to a wide-field illumination setup, resulting in a focal line in the front focal plane (object plane) of the objective. By tilting the scan mirror, the line is moved across the specimen (not depicted). The emission pathway of the *y*-direction is similar to the *x*-direction, with the exception that the light emerging from the points along the line are not descanned (*solid red line*), thus forming an image of the line on the CCD array. The *z*-position (position of the objective) is controlled by a piezo-driven actuator. GF, glass fiber; SM, scan mirror; DM, dichroic mirror; CL, cylindrical lens; SL, scan lens; TL, tube lens; PA, piezo actuator; O, objective; S, specimen (object plane); CCD, ccd camera.

as a maximum *z*-projection as in Fig. 3 *c*. Superimposing these maps using different colors creates a multicolor labeling of the network (see Fig. 3 *f*). Within the imaged volume, we could measure distinct reference signals from as many as 190 ROIs (Fig. 3 *e*). Assigning each of the corresponding correlation maps a distinct color allows an almost complete visualization of many neurons and their processes (Fig. 3 *g*). As the assignment of color is completely arbitrary, it is possible to highlight different features of the network by applying different color tables. For example, we can selectively highlight multiple (Fig. 3 *h*) or a single (Fig. 3 *i*) ensemble of neurons to visualize how these neurons are embedded in their surrounding circuitry. Finally, we can perform volume rendering and visualize all the obtained information as 3D movies (Movies S1 and S2).

It is noteworthy that the neuronal activity patterns of these units are obtained from the functional imaging data. Combining the activity time traces with the deduced structural information reveals network structure and function in an unprecedented clarity (Movie S3).

ACI in 3D using conventional imaging methods

What if fast scanning is not possible, e.g., in most cases of confocal, two-photon or wide-field imaging? In these cases ACI can still yield the complete 3D network structure through a number of consecutive 2D measurements. We first acquired time series of conventional confocal images at different *z*-positions using a high resolution objective (40×/1.2). The gaps between adjacent *z*-planes were carefully chosen to be slightly smaller than the thickness of the optical slice to ensure some overlap. At a given *z*-position, the correlation map often revealed only a fraction and discontinuous part of the cell's processes (Fig. 4 *a1*). However, because of the overlap between optical slices, the same cells or the same dendritic compartments could be detected in adjacent *z*-planes, so that we could reliably select regions of interest belonging to the same cell in the next *z*-plane (Fig. 4 *a2*). This procedure allowed us to measure a new reference trace of the same cell and construct its correlation map at this *z*-position. Carrying out the same

procedure for all subsequent planes led to the desired correlation map of the first neuron in this observation volume including its 3D dendritic branching pattern (Fig. 4 *a* and *b*). The correlation maps of the other neurons in the volume were carried out the same way, and assigning a different color to each of them resulted in their multicolor visualization (Fig. 4 *c*).

ACI and dye injection

As our multicolor ''staining'' is the result of a cross correlation algorithm, its interpretation is less obvious than, e.g., a fluorophore staining. We therefore performed a number of control experiments to compare the correlation maps with the neuronal morphology as revealed by dye injections (40×/NA 0.8 W objective). To this end we generated a complete set of 3D correlation maps online, selected a particular neuron from one of the maps, and filled it with fluorescent tracer through a patch pipette. (This experiment may also serve to demonstrate our method can be used as an online-tool). Fig. 5 *a* shows the staining obtained after the pipette was detached from the cell, whereas Fig. 5 *b* shows the correlation map of this neuron. The overlay in Fig. 5 *c* confirms that the structures emerging from the soma of the selected neuron in the correlation map are indeed processes of this cell. We never observed structures in the correlation map that branched off from the selected neuron and were not visible in the injection image. Of course, the correlation maps revealed, by definition, additional somata and dendritic segments with highly correlated activity, whenever present.

Combined ACI and dye injection were performed in five cells. The comparison of the morphology of the investigated neurons resulted in the following numbers (dye injection/ACI): primary dendrites emerging from the soma and ending in a glomerulus, 6/6 (1–2 per cell); branching of dendrites (subbranches leaving the observation volume in some cases), 7/9 (1–3 per cell); further processes emerging from the soma (possibly axons), 3/5 (0–2 per cell).

Occasionally, very thin structures that were observable in the injection-labeled image were missing in the correlation map (see insets of Fig. 5, *a* and *b*, *arrowheads*). To address the question whether these thin processes were generally inaccessible to our technique, we performed ACI using a higher magnification objective (63×, NA 0.95 W). As can be seen in Fig. 5 *d*, the correlation maps of these experiments clearly revealed very thin dendritic structures showing that ACI can detect these structures as long as they exhibit correlated [Ca^{2+}] signals.

Computer simulations

What are the conditions for a high ACI contrast? As ACI exploits the ''correlatedness'' (i.e., degree of similarity) between signals to define functional modules, the contrast between modules is given by the degree of their ''uncorrelatedness''. Assume the signals of the pixels belonging to a given neuron are scaled versions of the reference signal plus recording noise. If the noise is sufficiently large, there is a certain probability that a pixel's signal becomes more correlated to a ''wrong'' neuron. In this case, correlation analysis would not retrieve the correct affiliation of this pixel to its neuron. The probability of this error (in the sense of erroneous classification) depends on the pixels' SNR, but also on the correlation between the activities of the two neurons.

To objectively assess this dependency we performed computer simulations. Fig. 6 shows the error probability as a function of the SNR for a number of different inter-cell-correlations (ICC), defined as the correlation coefficient between the reference signal and the signal of the most correlated cell. At a given SNR, a lower ICC value markedly decreases the error probability (Fig. 6). The ICC values can be experimentally determined for any particular network and under the relevant experimental conditions. For the experiments in the *X. laevis* OB, for example, we determined an ICC of 0.08 ± 0.27 (mean $\pm$ SD for 50 s of spontaneous activity at 2 Hz, $n = 9180$ pairs). Our simulation results then indicate the minimum SNR (determined by laser power, exposure time, and the number of images) that is required to generate the desired ACI contrast.

DISCUSSION

ACI can generate a virtually unlimited number of correlation maps in a single experiment, and coding each of them with a different color results in a multicolor visualization of the complete neuronal network.

Recently, multicolor visualization of neuronal networks has been realized using a transgenic approach (1). In the *Brainbow* transgenic mice, a differential expression of two to four different fluorescent proteins is used to provide the contrast to distinguish neurons. Each neuron in *Brainbow* is thus coded by two to four variables, each representing the expression level of a particular fluorescent protein. ACI takes a different and partly complementary approach. We stain neurons with a single fluorescent dye but exploit the neurons' specific temporal activity waveforms as a contrast variable. In this way, each neuron is ''labeled'' by an N-dimensional temporal activity waveform, with N being the number of sample points in time. As we could increase the number of time points (limited only by bleaching), ACI provides a very high specificity to distinguish neurons. This property is manifested by the fact that individual correlation maps typically reveal only one or a few neurons and their processes with little unspecific labeling. A further advantage of obtaining contrast in the ''time domain'' is that it leaves the unused spectral channels available for other potential applications. For example, one might use fluorescent dyes of different colors to label the expression of certain proteins or molecules. This labeling would make it possible

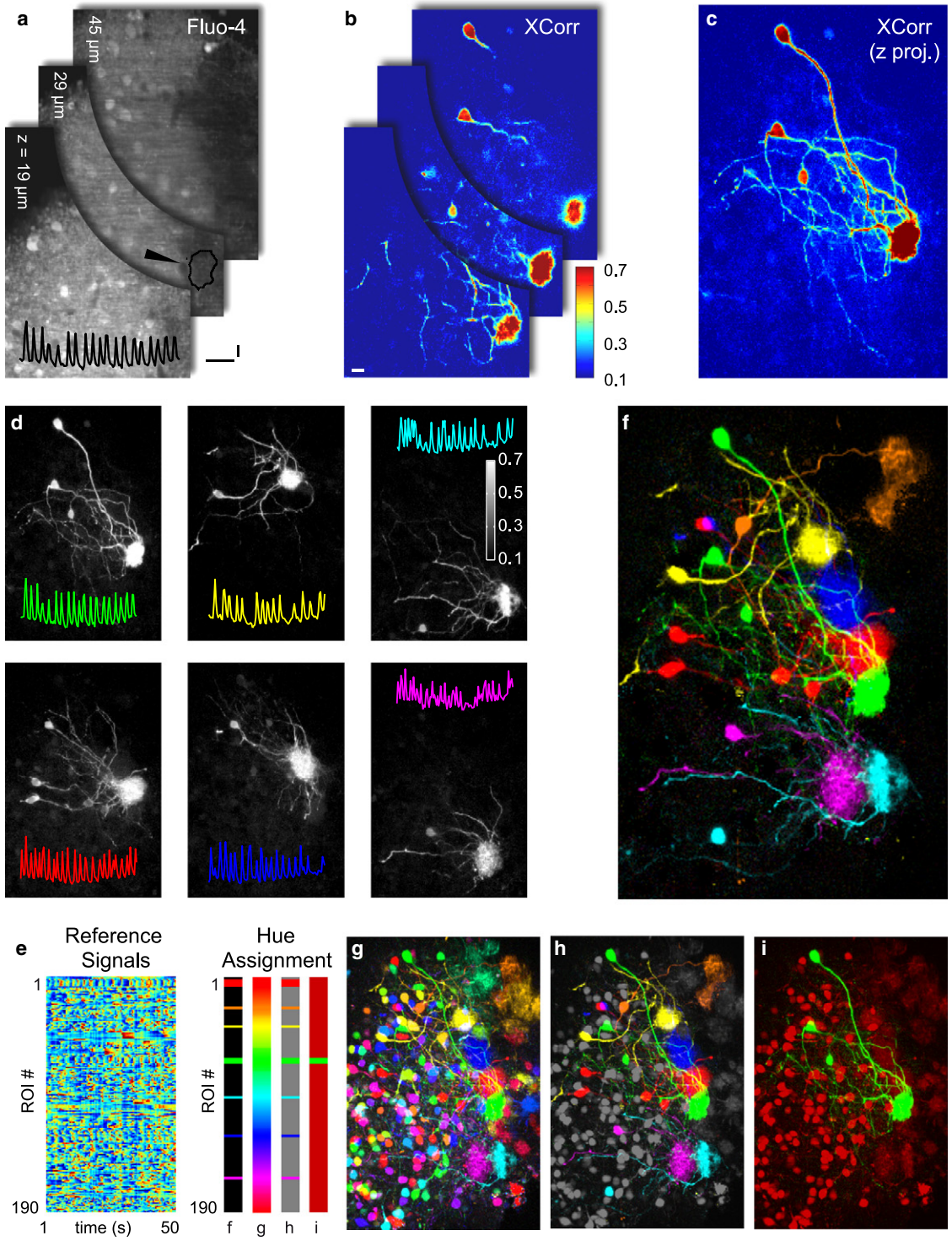

FIGURE 3 ACI together with fast confocal 3D scanning reveals network function and structure. (*a*) Mean projections over time of raw intensity images for three different *z*-positions as indicated. Superimposed are a region of interest (*arrowhead*) placed on a glomerulus and its corresponding time trace, taken as reference trace. Vertical scale bar 10% of $\Delta F/F_0$, horizontal scale bar refers to time trace (10 s). For length scale see *b*. (*b*) By applying the proposed correlation analysis to time series of image stacks, we obtained stacks of correlation maps as those presented in Figure 1. Shown are 3 out of 18 correlation maps at the *z*-positions indicated in *a*. The maps are based on correlation coefficients calculated with respect to the reference time trace. The colorbar codes the correlation values of the map. Scale bar, 10 μm, applies also to *a*. (*c*) Maximum *z*-projection reveals the morphology of the neurons belonging to this functional unit. Due to the sparseness of the functional labeling, the processes are clearly identifiable and the connectivity between somata and glomerulus is obvious. Same colormap as *b*. (*d*) By choosing reference traces from other ROIs (same experiment), multiple correlation maps were generated. Shown are six examples (each being a maximum *z*-projection like the one in *d*). All maps are scaled to the same interval used in *b* as indicated by the colorbar. (*e*) Left, [Ca^{2+}] signals of 190 different

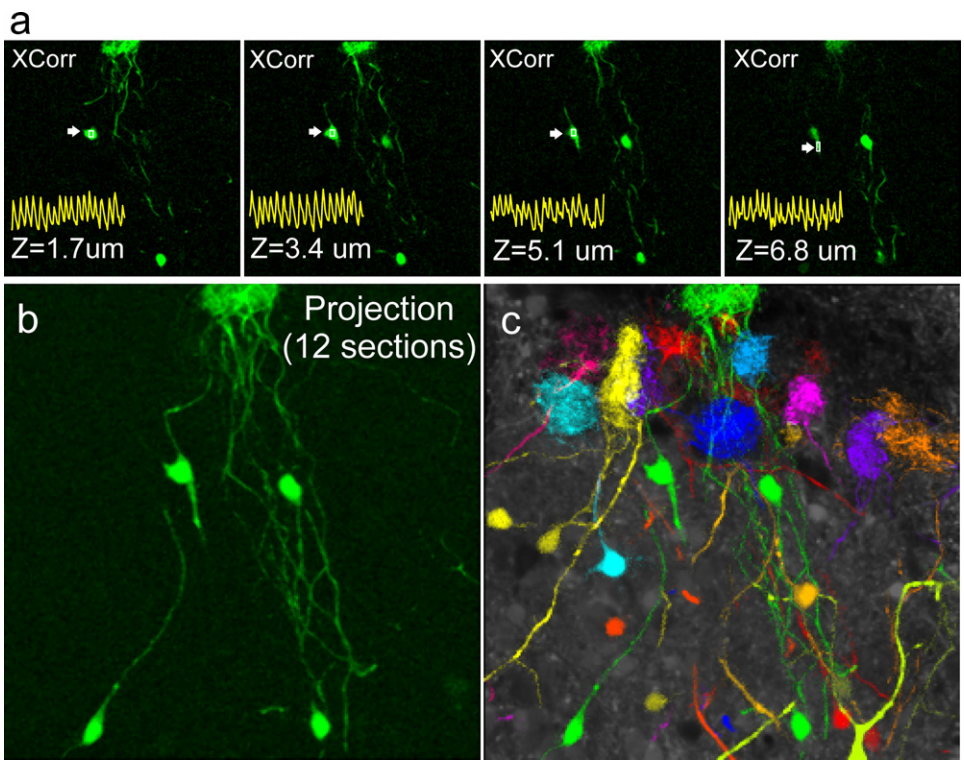

FIGURE 4 ACI in 3D using a conventional confocal laser scanning microscope. (*a*) Correlation maps of one neuron at different *z*-positions reconstructed by sequentially acquiring time series of confocal images at different *z*-planes. An overlap between optical slices allows the selection of ROIs (*arrows*) belonging to the same cell at different *z*-planes. The reference signals used to generate the corresponding correlation maps are superimposed. (*b*) Maximum z-projection of the correlation maps of this cell. (*c*) Multicolor visualization of the network structure resulting from the superposition of the correlation maps of different neurons.

to simultaneously map the expression of molecules, the expression of functional activities, and the morphology of neurons.

ACI develops its full potential when combined with a fast image acquisition system. Recently, a number of fast 3D imaging systems have been developed on the basis of point scanning through a predefined trajectory (16), AOD scanning (17,18), or planar illumination (19). Combined with bolus loading of [Ca^{2+}] indicators, these systems allow the imaging of many neuronal somata distributed in 3D. To visualize dendritic structures, however, the labeling density must be reduced, e.g., by electroporation (6) or by single cell dye injections. But this intrinsically limits the number of neurons that can be imaged to at most a few percent of all neurons. In contrast, the ACI approach provides the simultaneous visualization of both the functional activities and the dendritic connections of virtually all active and dye-loaded neurons in the volume of interest.

We performed ACI in the OB taking its spontaneous activities as the basis. Spontaneous activity has been recorded by use of calcium indicator dyes in many parts of the brain, including the cortex (20,2,21) and the hippocampus (22). In most cases the spontaneous activity time course was complex and synchronicity was sparse. Obviously, ACI could also be based on evoked activity, as long as the subset of activated neurons is either sparse or inhomogeneous with respect to the temporal response patterns.

It should be noted that the correlation map reveals the parts of an image that exhibit changes in fluorescence similar to the selected ROI. This might be a group of neurons, an entire neuron, or a subcompartment of a cell. In cell types where there is a strong action potential back-propagation into the dendritic tree (e.g., mitral cells, (23,24); pyramidal neurons or substantia nigra dopaminergic neurons, (25)), the correlation map is likely to reveal a substantial part of the cell, as we have shown here for the case of mitral cells. ACI may also be useful to study cell types where action potential back-propagation is relatively weak (e.g., Purkinje neurons, (25)). In these cases one might use the signals from different dendritic segments as reference signals to construct complementary correlation maps. This might reveal the whole cell's morphology but also the extent of functional subcompartmentalization within a single neuron and thus help to elucidate how these neurons integrate and process information.

Whereas compartmentalization of fluorescent dye in organelles was not an issue for the performance of ACI in our preparation, it might potentially affect the results of the ACI algorithm. It might prove beneficial to place the reference ROIs in organelle-free parts of the cell (e.g., periphery of the soma or olfactory glomerulus) and to minimize

ROIs, arranged as a matrix with time in *x*- and ROI index in *y*- direction. Color code of the time traces, dark blue to light red for low to high [Ca^{2+}], respectively. Right, four different color lookup tables chosen to highlight different features of the network. (*f–i*) Combining the correlation maps of different ROIs using the corresponding color lookup tables in *e*. In these maps, the hue of each pixel is determined by the hue of the ROI that most correlate to the pixel's signal. The intensity was determined by the degree of correlation.

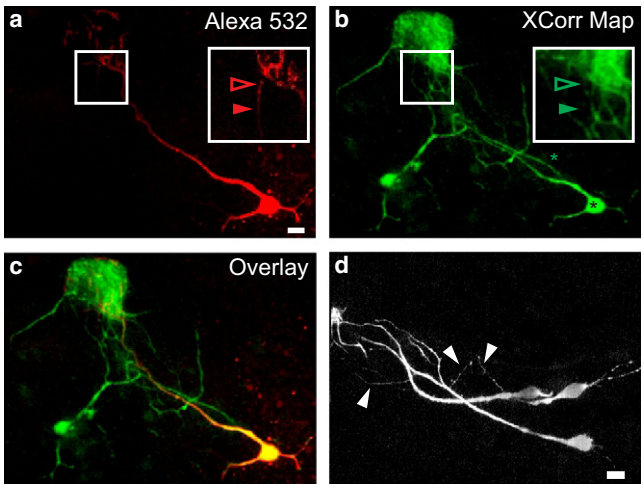

FIGURE 5 ACI and dye injection. (*a*) Intensity image after dye injection with a patch pipette (Alexa 532). The neuron's processes that are visible in the correlation map *b* are all present here. Some dendrites appear only very faint, indicating their small diameter (*inset*, *empty* and *solid arrowheads*). The inset is a projection of only three out of 24 *z*-planes. Scale bar 10 μm. (*b*) From this correlation map, the soma was selected for dye injection (*black star*). The inset shows a magnification of the indicated part (same as in *a*), with the empty arrowhead pointing at a part of a dendrite that disappears into noise (*solid arrowhead*). The marked dendrite (*green star*) does not belong to the solid neurons and only seems to branch off of the primary dendrite due to the depicted projection of the image stack. (*c*) The overlay of the correlation map with the injection image confirms that the majority of the structures is present in both images. (*d*) Correlation map acquired with a higher magnification objective. Thin secondary dendrites can be identified unambiguously (*solid arrowheads*). Scale bar 10 μm.

compartmentalization by optimizing the experimental parameters, such as the incubation temperature and the choice of the calcium indicator dye (for a review, see 26).

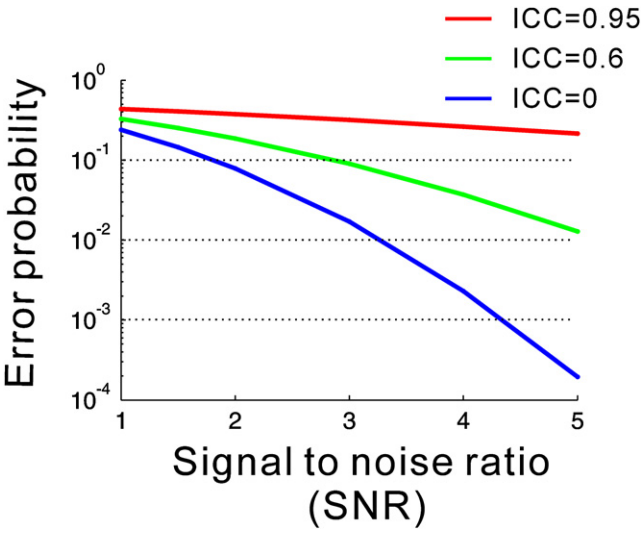

FIGURE 6 Specificity of ACI. The probability that a pixel's signal becomes more correlated to a "wrong" neuron as a function of SNR for three values of ICC. The ability to define the identity of a pixel increases (i.e., error probability decreases) as SNR becomes larger or the correlation between neurons (ICC) becomes smaller.

An additional strength of the method is that the computation of correlation maps can be done very fast. Using MATLAB on a common PC, we have been able to calculate 190 correlation maps (512 $\times$ 256 $\times$ 18 pixels each, 112 time points, Fig. 5) in 30 s, which is within the time for acquiring the actual data. The ability to map function and structure of neuronal populations online opens up a number of intriguing applications. It allows selecting specific cells (Fig. 5) or cell pairs (27) for targeted electrophysiological recordings. Further applications might include selecting neurons with certain functional and/or projection profiles for targeted ablation or stimulation. This way it will be possible to investigate how these changes affect the network function.

Taken together, ACI opens up novel ways for investigating and manipulating neuronal networks with an unprecedented specificity.

SUPPORTING MATERIAL

One figure and three movies are available at http://www.biophysj.org/biophysj/supplemental/S0006-3495(09)00563-3.

We thank Dr. A. Zeug and Dr. B.J. Lin for many fruitful discussions and scientific input. We also thank W. Mesecke, T. Nägel, and D. Governatori for advice and expert technical help with the construction of the line-scanning microscope.

D.S. suggested the topics of this project and supervised it. T.-W.C conceived the ACI principle, implemented the algorithms, performed computer simulations, and carried out the experiments in the conventional microscopes. S.J. designed the line-scan setup and built and characterized it together with M.A. The injection experiments were done by S.J., and the 3D volume scanning experiments in the line-scan setup were carried out by S.J. and TWC.

This project was funded by the DFG Center for Molecular Physiology of the Brain (Exc171, D.S.), by the Bernstein Center for Computational Neuroscience (S.J.), by a Carl Zeiss MicroImaging stipend (M.A.), and by the International Neuroscience M.Sc./PhD.–Program, Göttingen (Lichtenberg stipend to T.W.C.).

REFERENCES

1. Livet, J., T. A. Weissman, H. Kang, R. W. Draft, J. Lu, et al. 2007. Transgenic strategies for combinatorial expression of fluorescent proteins in the nervous system. *Nature*. 450:56–62.
2. Stosiek, C., O. Garaschuk, K. Holthoff, and A. Konnerth. 2003. In vivo two-photon calcium imaging of neuronal networks. *Proc. Natl. Acad. Sci. USA*. 100:7319–7324.
3. Ohki, K., S. Chung, Y. H. Ch'ng, P. Kara, and R. C. Reid. 2005. Functional imaging with cellular resolution reveals precise micro-architecture in visual cortex. *Nature*. 433:597–603.
4. Ohki, K., S. Chung, P. Kara, M. Hubener, T. Bonhoeffer, et al. 2006. Highly ordered arrangement of single neurons in orientation pinwheels. *Nature*. 442:925–928.
5. Garaschuk, O., R. I. Milos, and A. Konnerth. 2006. Targeted bulk-loading of fluorescent indicators for two-photon brain imaging in vivo. *Nat. Protocols*. 1:380–386.
6. Nagayama, S., S. Zeng, W. Xiong, M. L. Fletcher, A. V. Masurkar, et al. 2007. In vivo simultaneous tracing and Ca2+ imaging of local neuronal circuits. *Neuron*. 53:789–803.
7. Nieuwkoop, P. D., and J. Faber. 1967. Normal Table of Xenopus laevis. North Holland, Amsterdam.

8. Lin, B. J., T. W. Chen, and D. Schild. 2007. Cell type-specific relationships between spiking and [Ca2+]i in neurons of the Xenopus tadpole olfactory bulb. *J. Physiol.* 582:163–175.
9. Czesnik, D., W. Rossler, F. Kirchner, A. Gennerich, and D. Schild. 2003. Neuronal representation of odourants in the olfactory bulb of Xenopus laevis tadpoles. *Eur. J. Neurosci.* 17:113–118.
10. Manzini, I., C. Brase, T. W. Chen, and D. Schild. 2007. Response profiles to amino acid odorants of olfactory glomeruli in larval Xenopus laevis. *J. Physiol.* 581:567–579.
11. Chen, T.W. 2008. A system level analysis of neuronal network function in the olfactory bulb: coding, connectivity, and modular organization. PhD Thesis. University of Göttingen, Göttingen, Germany.
12. Chen, T. W., B. J. Lin, E. Brunner, and D. Schild. 2006. In situ background estimation in quantitative fluorescence imaging. *Biophys. J.* 90:2534–2547.
13. Sheppard, C. J. R., and X. Q. Mao. 1988. Confocal microscopes with sSlit apertures. *J. Mod. Opt.* 35:1169–1185.
14. Masters, B. R., and A. A. Thaer. 1994. Real-time scanning slit confocal microscopy of the in-vivo human cornea. *Appl. Opt.* 33:695–701.
15. Im, K. B., S. M. Han, H. Park, D. Kim, and B. M. Kim. 2005. Simple high-speed confocal line-scanning microscope. *Opt. Express.* 13:5151–5156.
16. Gobel, W., B. M. Kampa, and F. Helmchen. 2007. Imaging cellular network dynamics in three dimensions using fast 3D laser scanning. *Nat. Methods.* 4:73–79.
17. Reddy, G. D., and P. Saggau. 2005. Fast three-dimensional laser scanning scheme using acousto-optic deflectors. *J. Biomed. Opt.* 10: 064038.
18. Vucinic, D., and T. J. Sejnowski. 2007. A compact multiphoton 3D imaging system for recording fast neuronal activity. P*LoS. ONE.* 2:e699.
19. Holekamp, T. F., D. Turaga, and T. E. Holy. 2008. Fast three-dimensional fluorescence imaging of activity in neural populations by objective-coupled planar illumination microscopy. *Neuron.* 57:661–672.
20. Mao, B. Q., F. Hamzei-Sichani, D. Aronov, R. C. Froemke, and R. Yuste. 2001. Dynamics of spontaneous activity in neocortical slices. *Neuron.* 32:883–898.
21. Ikegaya, Y., G. Aaron, R. Cossart, D. Aronov, I. Lampl, et al. 2004. Synfire chains and cortical songs: temporal modules of cortical activity. *Science.* 304:559–564.
22. Usami, A., N. Matsuki, and Y. Ikegaya. 2008. Spontaneous plasticity of multineuronal activity patterns in activated hippocampal networks. *Neural Plast.* 2008:108969.
23. Bischofberger, J., and P. Jonas. 1997. Action potential propagation into the presynaptic dendrites of rat mitral cells. *J. Physiol.* 504:359–365.
24. Charpak, S., J. Mertz, E. Beaurepaire, L. Moreaux, and K. Delaney. 2001. Odor-evoked calcium signals in dendrites of rat mitral cells. *Proc. Natl. Acad. Sci. USA.* 98:1230–1234.
25. Stuart, G., N. Spruston, B. Sakmann, and M. Hausser. 1997. Action potential initiation and backpropagation in neurons of the mammalian CNS. *Trends Neurosci.* 20:125–131.
26. Takahashi, A., P. Camacho, J. D. Lechleiter, and B. Herman. 1999. Measurement of intracellular calcium. *Physiol. Rev.* 79:1089–1125.
27. Chen, T. W., B. J. Lin, and D. Schild. 2009. Odor coding by modules of coherent mitral/tufted cells in the vertebrate olfactory bulb. *Proc. Natl. Acad. Sci. USA.* 106:2401–2406.